

Low-ionization structures in planetary nebulae – IV. The molecular hydrogen counterpart

M. B. Mari^{1,2}, S. Akas³, and D. R. Gonçalves⁴

¹ Universidad Nacional de Córdoba, Observatorio Astronómico de Córdoba, Laprida 854, X5000BGR Córdoba, Argentina
e-mail: mbmari@unc.edu.ar

² Consejo Nacional de Investigaciones Científicas y Técnicas (CONICET), Godoy Cruz 2290, CABA, CPC 1425FQB, Argentina

³ Institute for Astronomy, Astrophysics, Space Applications and Remote Sensing, National Observatory of Athens, Penteli GR 15236, Greece

⁴ Observatório do Valongo, Universidade Federal do Rio de Janeiro, Ladeira Pedro Antonio 43, Rio de Janeiro 20080-090, Brazil

Received XXXXXX, XXXX; accepted XXXXXX, XXXX

ABSTRACT

Context. Low-ionization structures (LISs), found in all morphological types of planetary nebulae (PNe), are small-scale features prominent in emission from low-ionization species such as [N II], [S II], [O II] and [O I]. Observational and theoretical efforts have aimed to better understand their origin and nature. Recently, the detection of molecular hydrogen (H₂) emission associated with LISs in a few PNe has added a new piece to the puzzle of understanding these nebular structures.

Aims. Although observational studies indicate that LISs are characterized by lower electron densities than their host PNe, model predictions suggest higher total densities in these structures. The detection of H₂ emission from LISs in more PNe could help reconcile the observations with model predictions.

Methods. Observations of five PNe with already known LISs were conducted using the Near InfraRed Imager and Spectrometer (NIRI) mounted on the 8 m Gemini North telescope. A narrow band filter, centered on H₂ 1-0 2.122 μ m emission line, was used along with a continuum filter, to ensure continuum subtraction.

Results. We present a deep, high-angular resolution near-IR narrowband H₂ 1-0 S(1) imaging survey of five Galactic PNe with LISs. We nearly double the sample of LISs detected in the H₂ 1-0 2.122 μ m emission line as well as the number of host PNe. These findings allows us to prove that the systematically lower electron density in LISs – relative to the rims and shells of their host nebulae – is linked to the presence of H₂ molecular gas. Additionally, we provide the first estimation of the excited H₂ molecular mass in LISs, which is found between 200 and 5000 times lower than the corresponding ionized gas mass.

Key words. ISM: molecules, ISM: jets and outflows, photon-dominated region (PDR), planetary nebulae: individual: NGC 2392, NGC 6751, NGC 6818, NGC 6884, NGC 7354

1. Introduction

As a low- or intermediate-mass star consumes its fuels, and it approaches the end of the evolutionary journey of its life, it ejects the outer layers of material into the interstellar medium, leaving behind a hot and luminous core. The radiation field of the exposed core peaks in the ultraviolet (UV) range, resulting in the dissociation of molecular gas formed in the previous stage of asymptotic giant branch (AGB) star and then in the ionization of atomic gas. These processes form the bright, and colourful planetary nebulae (PNe) we observe, which are among the most important contributors to the chemical enrichment of the interstellar medium in galaxies.

PNe display a variety of shapes and morphologies like round, elliptical, bipolar and multipolar (e.g. Manchado et al. 1996). They are also characterized by distinct components such as rims, shells, and attached haloes prominent mostly in [O III] and hydrogen recombination lines (Balick & Frank 2002). Besides, it is also known that PNe display structures in smaller scales prominent in emission from low-ionization species such as N⁺, S⁺, O⁺ or O⁰ (e.g. Corradi et al. 1996; Balick et al. 1998; Gonçalves et al. 2001).

Many efforts have been made to decipher the nature of these low-ionization structures (hereafter LISs) and their unforeseen

low electron density relative to the surrounding gas (see e.g. Balick et al. 1994; Hajian et al. 1997; Gonçalves et al. 2003, 2004, 2009; Akas & Gonçalves 2016; Danekhar et al. 2016; Ali & Dopita 2017; Monreal-Ibero & Walsh 2020; Miranda et al. 2021; Akas et al. 2022; Mari et al. 2023b). Recently, Mari et al. (2023a) probed the physico-chemical properties of LISs and host PNe, conducting a statistical analysis for a sample of 33 PNe containing 88 rims/shells and 104 LISs, and verified that neither the chemical abundances nor the electron temperatures show significant differences from one to another component. However, LISs correspond to a group of nebular structures statistically different from the rims and attached shells of the host nebula in terms of electron density (n_e), having two-thirds lower n_e (~ 1700 cm⁻³) than other nebular components (~ 2700 cm⁻³), with interquartile ranges (25th to 75th percentiles) of 800-2700 cm⁻³ and 1800–5000 cm⁻³, respectively.

O'Dell & Handron (1996) discussed the origin of the cometary knots in the well-studied Helix Nebula, suggesting that Rayleigh–Taylor instabilities during the early PN phase are the most likely cause, although a primordial origin linked to the central star's formation cannot be ruled out. Other authors have also suggested similar formation mechanisms to explain the origin of LISs, such as stagnation points (Steffen et al. 2001), Rayleigh-

Taylor instabilities (e.g. Ramos-Larios & Phillips 2009), AGB fossils (e.g. Gonçalves et al. 2001), among others. All these models require LIS' densities orders of magnitude higher than the surrounding nebular gas, typically $>10^4 \text{ cm}^{-3}$ (e.g., Raga et al. 2008; Balick et al. 2020). Gonçalves et al. (2009), in an attempt to reconcile the optical observations with theoretical models, proposed that a significant fraction of gas in LISs should be neutral (atomic and/or molecular) and thus hidden for the visible light observational studies.

The high total (i.e., electron, neutral and molecular) density is a necessary condition for preventing molecular hydrogen (H_2) dissociation. The presence of H_2 in PNe is already well known, particularly in bipolar PNe (Gatley's rule, e.g. Kastner et al. 1996), mainly through observations of the ro-vibrational emission line $\text{H}_2 \text{ v}=1-0 \text{ S}(1)$, centred at $2.122 \mu\text{m}$. The Helix Nebula, one of the brightest and closest planetary nebulae to Earth, was among the first to provide evidence of H_2 associated with knotty structures, enabling comprehensive investigations of its cometary knots through both observational and modeling approaches (O'Dell & Handron 1996; O'Dell et al. 2000; López-Martín et al. 2001; Meixner et al. 2005; Hora et al. 2006; Mat-suura et al. 2009).

It was not long ago that the presence of H_2 was also verified in other microstructures embedded in PNe, as LISs. In this context, it is worth mentioning that an empirical linear correlation between the $[\text{O I}] \lambda 6300$ and $\text{H}_2 \text{ 1-0 S}(1)$ emission-lines had already been demonstrated in early studies of PNe (Reay et al. 1988). Following the link between these two lines, Akras and collaborators selected LISs with strong $[\text{O I}] \lambda 6300$ emission and successfully detected the $\text{H}_2 \text{ 2.122} \mu\text{m}$ line in several of them: K 4-47 and NGC 7662 (Akras et al. 2017), as well as NGC 6543 and NGC 7009 (Akras et al. 2020). Two additional PNe with H_2 -emitting knots have also been reported: Hu 1-2 (Fang et al. 2015) and Hb 12 (Fang et al. 2018).

Aleman & Gruenwald (2011) showed that H_2 is confined to a narrow region between the point where the ionized hydrogen fraction reaches 95% and the outer boundary of the ionized region, where this fraction drops to 0.01%. Within this transition zone, the peak of the emissivity of the $\text{H}_2 \text{ 2.122} \mu\text{m}$ line is found, along with those of low-ionization lines ($[\text{N II}]$, $[\text{S II}]$, $[\text{O I}]$) (see their Fig. 4), with spatial separations that exceed the thickness of the ionization front. More recently, Akras et al. (2024) presented the first spatially resolved MUSE image of the atomic carbon line $[\text{C I}] \lambda 8727 \text{Å}$ in NGC 7009. This line originates only from the pairs of LISs suggesting the presence of high density, partially ionized gas. The same emission line has also been detected in the LISs of NGC 3242 suggesting that it could be another common characteristic of these microstructures (Konstantinou et al. 2025). García-Rojas et al. (2022) also presented the $[\text{C I}] \lambda 8727 \text{Å}$ MUSE map for a number of PNe. Examining the radial stratification of emission lines in the K1 LIS of NGC 7009 (Gonçalves et al. 2003), Akras et al. (2024) argued that photoevaporation of dense knots could explain the observations.

The ionization and photoevaporation of neutral clouds illuminated by the UV radiation of O and/or B stars were studied since long ago (Kahn 1954; Oort & Spitzer 1955), aiming to explain their acceleration. Years later, Bertoldi (1989); Bertoldi & McKee (1990) developed approximate analytical models for the evolution of neutral clouds. The photoevaporation of the cloud's gas results in the rocket effect causing the clouds to accelerate away from the ionizing source. In such neutral/molecular clouds, the ionization and photodissociation fronts are not necessarily separated, which is a key difference from classical photodissociation regions (PDRs) (Bertoldi & Draine 1996; Henney

et al. 2007). Subsequently, a number of theoretical and observational studies applied the photoevaporation mechanism to neutral clumps in PNe (e.g. Mellema et al. 1998; Raga et al. 2005), and to the cometary knots in Helix nebula (e.g. O'Dell et al. 2000; López-Martín et al. 2001; O'Dell et al. 2005). Nevertheless, LISs in PNe that do not show cometary morphology remain poorly understood, and the H_2 molecular component has only been observationally confirmed in a handful cases.

This pilot survey presents the H_2 emission line of a sample of LISs in PNe, covering a variety of LIS' types in PNe of different morphological classes. The main goal of this study is analyzing and quantifying the molecular H_2 gas content of LISs. The detection of H_2 emission exclusively associated with LISs also enables a comparison between the masses of ionized and molecular material. Such an analysis can provide a more accurate estimate of the amount of molecular mass, at least in its excited state, within the LISs. Through this approach, we aim to advance the understanding of a key discrepancy: while theoretical models predict significantly higher total densities in LISs compared to the rims/shells of their host PNe, optical observations indicate that the electron densities in LISs are at least two-thirds lower than those of the surrounding gas. This study will contribute to diminishing the gap between models and observations, providing crucial data to resolve this intriguing dichotomy.

In Section 2, we present the observed sample along with the data reduction and calibration. In Section 3, we show the results obtained from NIRI images. Section 4 provides the mass estimates and the relationship between ionized and excited molecular content. Finally, in Section 5 and 6, we present the discussion and overall conclusions.

2. Narrowband imaging observations

Aiming to prove the hypothesis that the presence of H_2 is a general characteristic of LISs and is therefore associated with different LISs classes – knots, filaments, jets, whether in pairs or isolated – we conducted very deep narrowband $\text{H}_2 \text{ 2.122} \mu\text{m}$ imaging for a sample of five PNe. Observations were carried out with the Near-Infrared Imager and Spectrometer (NIRI), mounted on the 8 m Gemini North telescope in Mauna Kea, Hawaii.

2.1. Data acquisition and reduction

The observations were conducted between July and October 2020 (Program ID: GN-2020B-Q-128, PI: S. Akras). The f/6 configuration, with a pixel scale of 0.117 arcsec and a FoV of 120 arcsec , was used since it is ideal for observing PNe with angular sizes smaller than 100 arcsec . The narrowband G0216 filter, with an effective width of $\sim 327 \text{ Å}$, centered at $2.1239 \mu\text{m}$, was used to isolate the $\text{H}_2 \text{ 1-0 S}(1)$ line at $2.122 \mu\text{m}$. For proper continuum emission subtraction, the G0217 filter, with an effective width of $\sim 329 \text{ Å}$, centered at $2.0975 \mu\text{m}$, was also employed. To increase the signal-to-noise ratio (S/N), several individual frames were obtained per object. The observations are detailed in Table 1. In agreement with the Gemini baseline calibrations, GCAL flat frames and dark frames with different times based on the science images were obtained to correct thermal emission, dark current and/or hot pixels. Standard stars (SAO34401, GSPC S813-D, FS 150 and FS 123) were also observed to flux calibrate the data.

Table 1. Observation log.

Object	Filter	# Combined frames	Exp.time [s]
NGC 2392	H ₂ v=1-0 S(1)	12	240
	K-cont	6	240
NGC 6751	H ₂ v=1-0 S(1)	12	180
	K-cont	8	180
NGC 6818	H ₂ v=1-0 S(1)	12	180
	K-cont	7	180
NGC 6884	H ₂ v=1-0 S(1)	11	200
	K-cont	6	200
NGC 7354	H ₂ v=1-0 S(1)	11	200
	K-cont	7	200

Notes. The H₂ v=1-0 S(1) narrowband filter isolates the molecular H line centered at $\lambda_c = 2.1239 \mu\text{m}$, whereas the K-cont filter ($\lambda_c = 2.0975 \mu\text{m}$) is used to map the continuum emission, thus allowing the continuum subtraction of the H₂ v=1-0 S(1) images.

Before starting data reduction, as recommended by Gemini¹, the PYTHON routines CLEARIR.py and NIRLIN.py were used. The first one is needed to remove artefacts as vertical striping and/or horizontal banding, whereas the latter corrects the non-linearity of the detector. The images were reduced using DRAGONS² (Data Reduction for Astronomy from Gemini Observatory North and South, Labrie et al. 2019), a PYTHON-based software for the Gemini data reduction, provided by the Gemini observatory. This software package can stack multiple dark observations to create a master dark. From the GCAL flats and short darks, a bad pixel mask (BPM) can be produced. A master flat can also be generated from multiple observations of lamps-on and lamps-off. Science data were then reduced considering the BPM, the corresponding master dark and the appropriate master flat field for each filter.

2.2. Flux calibration and continuum subtraction

Given the night-time atmospheric variations, the full width at half maximum (FWHM) of the background stars was not necessarily the same in both filters. Using background stars present in both images, we computed, per target, the average FWHM. The image with the smallest FWHM was degraded before proceeding with the subtraction of the continuum from the emission-line image. This was done employing the GAUSS task in IRAF, which convolves the image with an elliptical Gaussian function after specifying the sigma parameter.

Due to the lack of broadband K filter observations for the standard stars, we calculated their theoretical K magnitudes ($\text{Flux}_K^{\text{theoretical}}$) by modelling their blackbody spectral energy distributions (SEDs). For this end, we adopted effective temperatures derived from their spectral types and used the transmission curves of the filters. For flux calibration, we used the absolute K magnitudes of the standard stars ($\text{Flux}_K^{\text{standard star}}$) from the Two Micron All Sky Survey (2MASS; Skrutskie et al. 2006) for SAO34401 and from the UKIRT Infrared Deep Sky Survey (UKIDSS; Hambly et al. 2008) for GSPC S813-D, FS 150, and FS 123. From this, we derived the calibration factors ($\text{Flux}_K^{\text{standard star}}/\text{Flux}_K^{\text{theoretical}}$), which were then used to flux-calibrate the narrowband images of the targets obtained with

NIRI, applying the transmission curves of the corresponding filters.

For continuum subtraction in the flux-calibrated images, we first aligned the H₂ and K-cont images, using as many field stars as possible. Then, we computed the scale factor required for the proper subtraction of field stars in the emission-line frames. Specifically, we used the equation $\text{filter}_{H_2} - (H_2/K\text{-cont}) \times \text{filter}_{K\text{-cont}}$, where $(H_2/K\text{-cont})$ represents the scale factor. To estimate this factor, background stars present in both images were used, and their fluxes were compared. Fig.1 gives an example of the continuum-subtraction process, for which we apply different scale factors. A scale factor that is too small (insufficient) is imperceptible in the continuum subtraction, while excessively high values lead to oversubtraction, resulting in an underestimation of the H₂ fluxes.

Several uncertainties are involved in the process just described, including those due to: (i) the standard stars effective temperature used to obtain their theoretical SEDs; (ii) the conversion factors applied for the flux calibration of both standard stars and science targets; and (iii) the scale factor used for continuum subtraction, determined by ensuring satisfactory removal of field stars in the H₂ science images. Additionally, flux calibration is subject to an inherent photometric uncertainty of approximately 10% due to unmeasured atmospheric extinction³. Each of the quoted processes contributes with an uncertainty of roughly 10%, while these uncertainties may not be entirely independent. Moreover, both 2MASS and UKIRT report photometric errors of approximately 0.02-0.03 mag (Skrutskie et al. 2006; Lawrence et al. 2007, , respectively), resulting in a baseline flux calibration uncertainty of around ~3%. The combined effect of these uncertainties likely results in an overall uncertainty in the H₂ flux measurements of about 30-40%.

Despite these uncertainties, we anticipate that when comparing the parameter A in the relation $M_{H\text{ II}}/M_{H_2} = A/n_e \times F_{\text{Bry}}/F_{H_2}$ with values reported in the literature, we find a difference of only 13% (see Section 4.2 where we define and discuss the H II over H₂ mass ratio). This level of agreement suggests that, while uncertainties are significant, our flux calibration methodology produces reliable results.

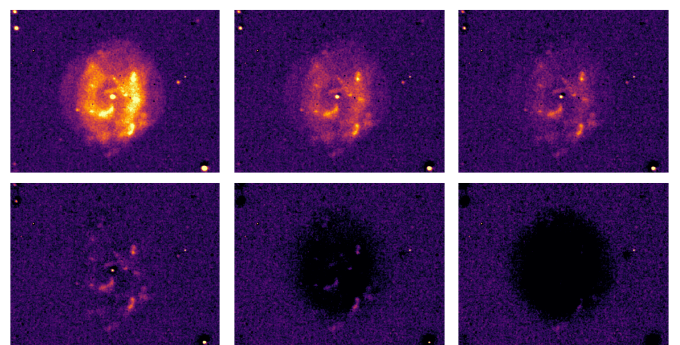


Fig. 1. Comparison of continuum-subtracted images that resulted from a variation of scale factors. From top to bottom and left to right, the scale factor increases (0.9, 1.0, 1.05, 1.1, 1.2, 1.3). Initially, the poor continuum subtraction is evident, since the field stars appear as H₂ line emitters (top panels). The last two bottom panels, are clear examples of over-subtraction of the continuum.

¹ <http://www.gemini.edu/instrumentation/niri/data-reduction>

² <https://dragons.readthedocs.io/en/stable/>

³ <https://www.gemini.edu/observing/resources/near-ir-resources>

3. Results: NIRI H₂ versus HST [N II] imagery

In this work, the first deep, spatially resolved and continuum-subtracted narrowband H₂ 2.122 μm images for the planetary nebulae NGC 2392, NGC 6751, NGC 6818, NGC 6884 and NGC 7354 are presented. The NIRI H₂ results are presented in comparison with HST [N II] images of this PNe sample, which facilitates the interpretation of our results.

3.1. NGC 2392

It is known that in addition to the multiple system of knotty and filamentary LISs, located at the inner part of its high-excitation shell, NGC 2392 also has a bipolar jet of high-velocity (150–185 km s⁻¹), directed almost toward the observer (O'Dell & Ball 1985; Giesekeing et al. 1985). Due to their orientation and low surface brightness, these jets are not detected in optical images and can only be distinguished in spatially resolved high-resolution [N II] spectra (see e.g. García-Díaz et al. 2012; Guerrero et al. 2021). In the central panel of Fig. 2, we present the narrowband continuum-subtracted H₂ 2.122 μm image of NGC 2392. Multiple knots and filaments are seen in the molecular hydrogen light. Panels (a), (b), (c) and (d) cover different regions of the nebula, and also display the contours of the [N II] $\lambda 6584$ emission from HST, overlaid on the NIRI H₂ 1–0 S(1) image NGC 2392. H₂ and [N II] lines show a very good spatial correlation, as it has been demonstrated in previous studies (Akras et al. 2017, 2020). The H₂ fluxes from five LISs are listed in Table 2, they range from 0.25 to 0.8×10^{-15} erg s⁻¹ cm⁻².

3.2. NGC 6751

Among its multitude of structures, this PN has a [N II] knotty ring and irregular filaments in the northeast quadrant of the halo (Chu et al. 1991; Clark et al. 2010). Figure 3 presents the continuum-subtracted H₂ images of NGC 6751. It can be seen that H₂ emission emanates from the inner parts of the nebula, where [N II] emission is evident. Faint H₂ emission is detected in the pairs of jet-like structures which are also detected in the [N II] line. The H₂ fluxes of the latter structures vary from 0.37 to 1.73×10^{-15} erg s⁻¹ cm⁻² (see Table 2). The filamentary structures of the halo exhibit stronger H₂ emission (upper left panel), with fluxes ranging from 1.85 to 3.84×10^{-15} erg s⁻¹ cm⁻². These findings further supports the Clark et al. (2010) idea that such filaments are remnants of AGB mass-loss events.

3.3. NGC 6818

In the light of [N II], NGC 6818 shows multiple filamentary structures distributed around the whole nebula, labeled as "moustaches" by Benetti et al. (2003). Our deep near-IR image of this nebula is presented in Fig. 4 along with the [N II] emission line contours from HST. H₂ 2.122 μm emission line is detected only in the LISs or "moustaches", prominent in [N II]. The H₂ flux based on three LISs varies between 1.44 and 2.88×10^{-15} erg s⁻¹ cm⁻² (see Table 2), which are among the brightest LISs in our sample.

3.4. NGC 6884

The [N II] image of NGC 6884 shows a pair of LISs in opposite direction with a radial velocity of 40 km s⁻¹ (Miranda et al. 1999), interpreted at that time as a precessing bipolar outflows. More recent, diffraction-limited and narrow-band HST images in the [N II] emission unveiled that the pair of knots is actually two symmetrical knotty arc-like structures (Palen et al. 2002). Figure 5 shows the continuum-subtracted H₂ 2.122 μm image of NGC 6884. In the left panel, we can observe that significant H₂ is detected for the time from the outer halo of this nebula, at distances up to 30–40 arcsec from the central star. Panels (a) and (b) present a zoom-in view of the central part of the nebula, where an arc-like structure is clearly detected in the eastern part. The H₂ (1–0) S(1) emission of this arc-like structure shows a spatial correlation with the [N II] emission from the HST data, but we cannot verify that H₂ emission originates from the knots due to the lower-spatial resolution of our data. The H₂ flux in two regions of the eastern arc-like ranges from 0.75 to 1.86×10^{-15} erg s⁻¹ cm⁻² (see Table 2), while regions in the outer halo exhibit fluxes between 2.60 and 18.35×10^{-15} erg s⁻¹ cm⁻². As in NGC 6751, the H₂ emission from halo structures in this object also seems to be related to remnants of mass-loss episodes during the AGB stage.

3.5. NGC 7354

Multiple microstructures prominent in [N II] emission have been identified and studied by a few authors in NGC 7354 (e.g., Hajian et al. 1997; Contreras et al. 2010), including the pair of jet-like LISs along its major axis. By using near- and mid-IR data from 2MASS and *Spitzer*, Phillips et al. (2009) studied NGC 7354. Due to the low spatial resolution of their data, the equatorial LISs and jet-like structures were not clearly detected. Nevertheless, all LISs are seen in our data (Fig. 6). The left panel presents the continuum-subtracted H₂ image of NGC 7354. The right panels (a), (b), (c) and (d) show the contours of [N II] emission superimposed on the H₂ zoom-in images of the LISs. There is a clear spatial correlation between the two emission lines. We also report the first detection of H₂ emission from the jet-like structures indicative of collisional excitation. The H₂ fluxes of four LISs vary from 1.35 to 2.68×10^{-15} erg s⁻¹ cm⁻² (see Table 2).

4. Results: molecular and ionized LISs' content

The primary motivation for studying LISs' emission in molecular hydrogen lines was to address the question: *Why do the vast majority of LISs exhibit electron densities lower than those of nebular rims and shells?* Since the latter contradicts theoretical predictions, we computed the molecular and ionized masses in LISs to examine whether their H₂ content helps alleviate the tension between observations and theory, as previously suggested by Gonçalves et al. (2009). Here, we integrate our results with data available in the literature.

4.1. Molecular hydrogen mass

After measuring the H₂ $\lambda 2.122$ fluxes for several LISs in our sample, we can also estimate their molecular hydrogen mass. For that we adopted Equation 1 from Scoville et al. (1982):

$$F_{H_2, \lambda 2.122} = \frac{n_{H_2} V_{H_2} f_{v=1, J=3} A_{S(1)} h\nu}{4\pi d^2} \quad (1)$$

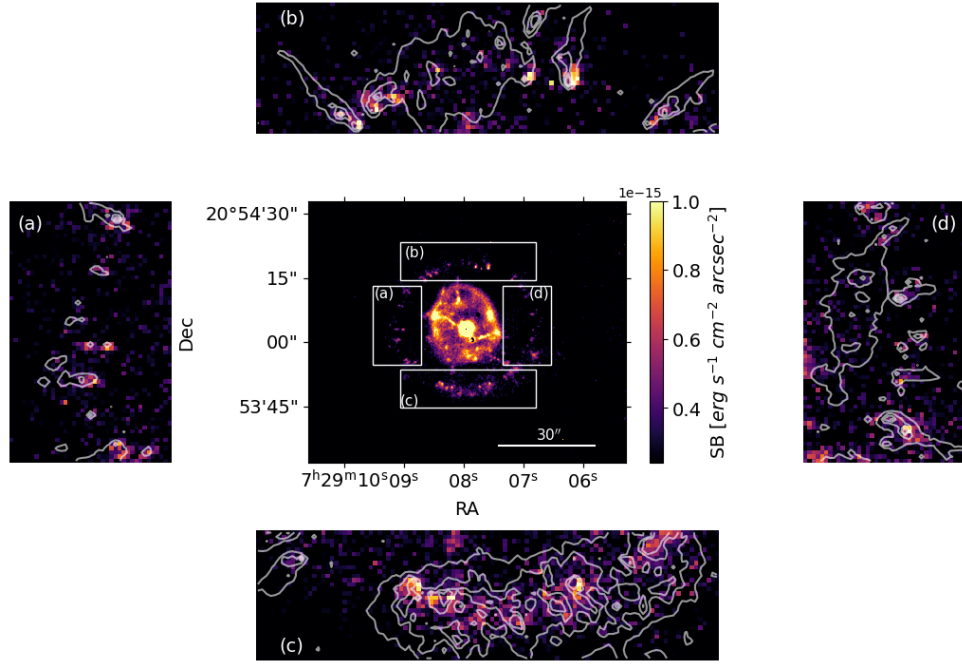


Fig. 2. Surface brightness (SB) of the H_2 1–0 S(1) continuum-subtracted image for NGC 2392 (center). Panels a, b, c, and d display the H_2 continuum-subtracted image overlaid with HST [N II] emission contours for different regions of the nebula.

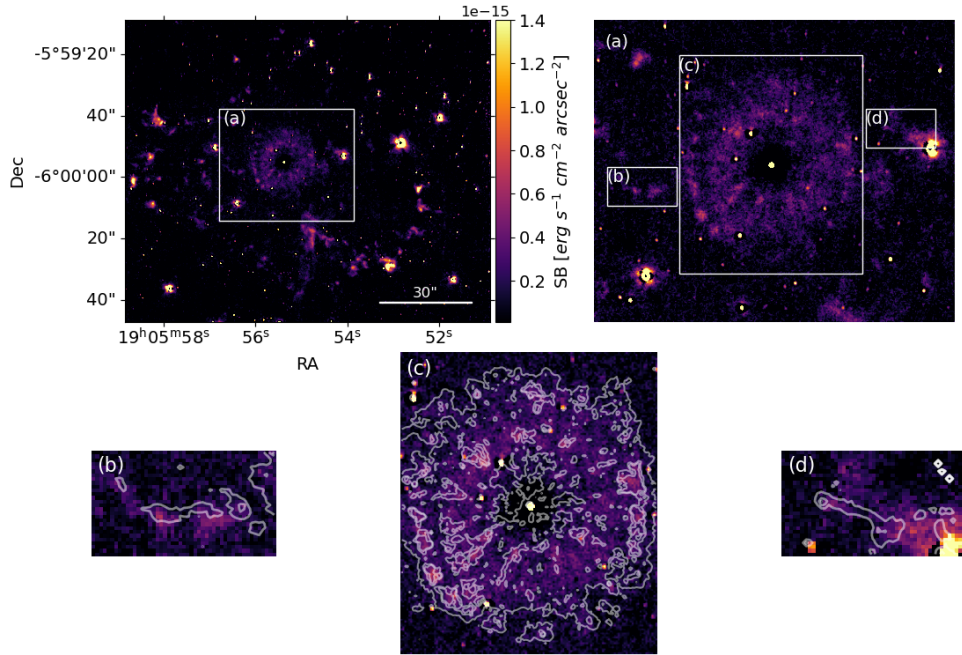


Fig. 3. Surface brightness (SB) of the H_2 1–0 S(1) continuum-subtracted image for NGC 6751. The upper-left panel displays the entire nebula, revealing faint emission from its halo at distances greater than 30 arcsec. The right panel (a) provides a zoomed-in view of the nebula’s center, showing the eastern and western jet-like structures along with numerous knots in the outer rim. The bottom panels present the continuum-subtracted H_2 image overlaid by the HST [N II] emission line contours: (c) focuses on the nebula’s center, while (b) and (d) display the pairs of the jet-like structures. The seemingly brilliant knot in the western jet-like structure is a background star.

where n_{H_2} is the H_2 volume density, V_{H_2} is the volume of the region that contains the H_2 gas, $A_{S(1)} = 3.47 \times 10^{-7} s^{-1}$ is the H_2 1–0 S(1) transition probability for temperature $T=2000$ K (Turner et al. 1977; Riffel et al. 2008), $f_{v=1, J=3} = 0.0122$ is the population fraction of H_2 in the $v=1, J=3$ level, d is the distance of the nebula, h is the Planck constant, and ν is the frequency of the H_2 line. Rearranging the above equation allows us to determine the mass of the H_2 component in LISs, which can be derived from:

$$M_{H_2} = \frac{2m_p F_{H_2 \lambda 2.122} 4\pi d^2}{f_{v=1, J=3} A_{S(1)} h \nu} \quad (2)$$

$$\sim 5.0776 \times 10^7 \left(\frac{F_{H_2 \lambda 2.122}}{erg \ s^{-1} cm^{-2}} \right) \left(\frac{d}{kpc} \right)^2 [M_\odot]$$

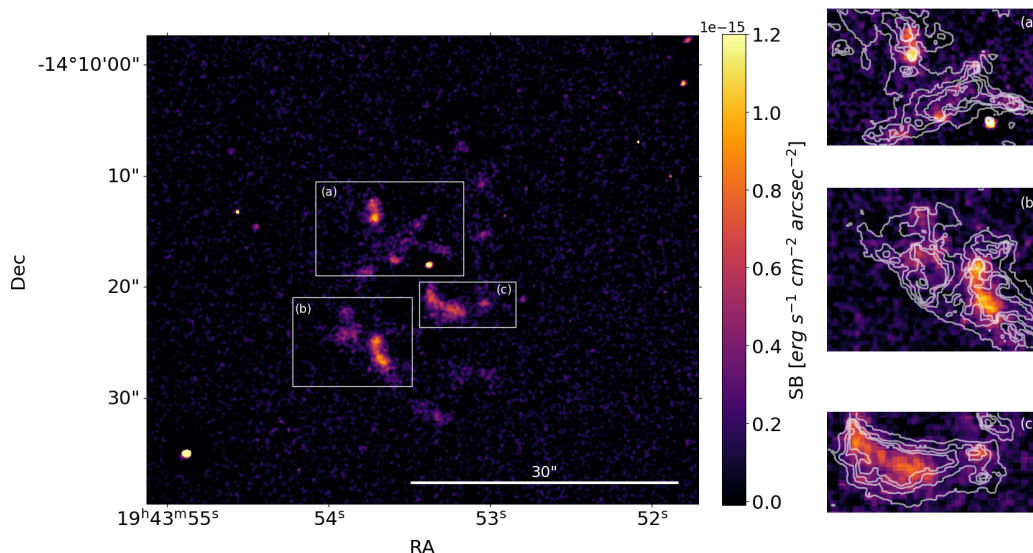


Fig. 4. Surface brightness (SB) of the H_2 1–0 S(1) continuum-subtracted image for NGC 6818 is shown in left panel. The other panels present the H_2 continuum-subtracted image overlaid with HST [N II] emission contours, highlighting three regions of the nebula: (a) and (b) correspond to the "moustache" structures, while (c) is the brighter southern part of the nebula.

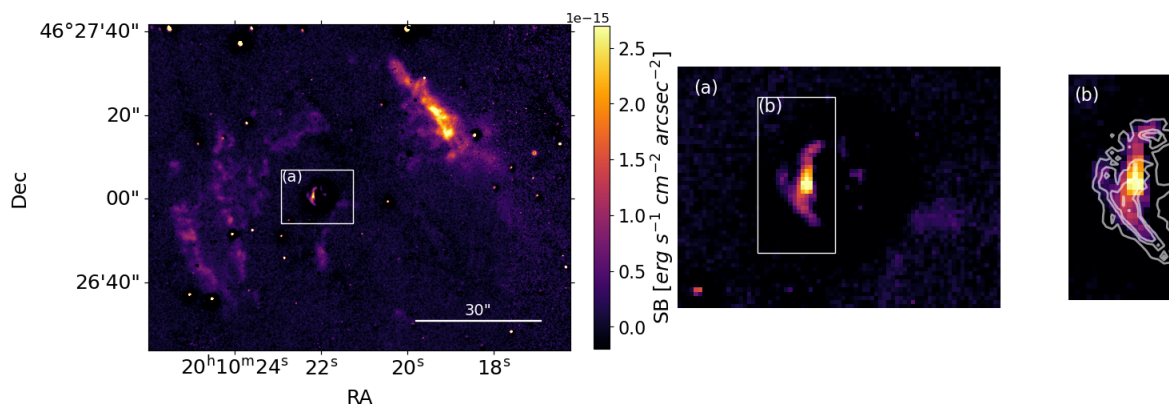


Fig. 5. Surface brightness (SB) of the H_2 1–0 S(1) continuum-subtracted image for NGC 6884 is shown in left panel. The center panel provides a zoomed-in view of the entire nebula, while the other two panels display the H_2 continuum-subtracted image overlaid with HST [N II] emission contours, highlighting the knotty arc-like structure in a half region of the nebula, labeled as (b) and (c).

where m_p is the mass of the proton and $F_{\text{H}_2 \lambda 2.122}$ is the observed flux of the emission line (Diniz et al. 2015).

Since it requires an external energy source to excite the ro-vibrational levels of the H_2 molecule, such as UV photons from the central star or shock waves, the flux from the $\text{H}_2 \lambda 2.122$ line does not represent the distribution of the cold molecular component. Represently, our data trace the highly excited H_2 gas, referred to as the *warm* H_2 component, and therefore the masses estimated from the aforementioned equation correspond to this component. Thus, the masses computed and presented in this work represent the lower limits of the total H_2 mass in LISs.

Table 2 encompasses the first estimations of the *warm* H_2 masses for 19 LISs in our sample of five PNe. These masses range from 0.4 to $10 \times 10^{-7} M_\odot$, with an average of $4.6 \times 10^{-7} M_\odot$. Given that Equation 2 is commonly applied to active galactic nuclei (AGN; e.g., Reunanen et al. 2002; Diniz et al. 2015), we also computed the H_2 mass of the cometary knot K1 (RA:22:29:33.41, Dec:-20:48:04.73) in the Helix planetary nebula using the same equation to ensure the reliability of our estimates. This procedure resulted in a H_2 mass for K1 of $\sim 3.9 \times 10^{-8} M_\odot$ that is one order of magnitude smaller than the

H_2 masses in the LISs of our PNe sample. Nevertheless, our measurement of the H_2 mass for K1 is reasonably in agreement with that provided by Matsuura et al. (2007) through near-IR IFU observations (see Table 2). The detection of several H_2 lines from different ro-vibrational states allowed the authors to construct the excitation diagram and determine the excitation temperature and column density of the H_2 gas from a robust approach, resulting in $\sim 2 \times 10^{-8} M_\odot$, which is half of the value we obtained. Considering the different type of data, the uncertainties in the H_2 fluxes (discussed in Section 2.2), and the fact we adopted the distance to the nebula from Gaia DR3 parallaxes (Gaia Collaboration et al. 2023; Bailer-Jones et al. 2021), only available more recently, we argue that our methodology provides adequate and reliable warm H_2 masses for the LISs.

Wesson et al. (2024) also provided an H_2 mass for the globules of NGC 6720, using data from the JWST Early Release Observations. The authors used the same approach as De Marco et al. (2022) for NGC 3132. The extinction of the knots in the IR wavelength regime was derived by assuming the extinction law from Cardelli et al. (1989). This led first to the estimation of the column density, and then the total H density and H_2 mass.

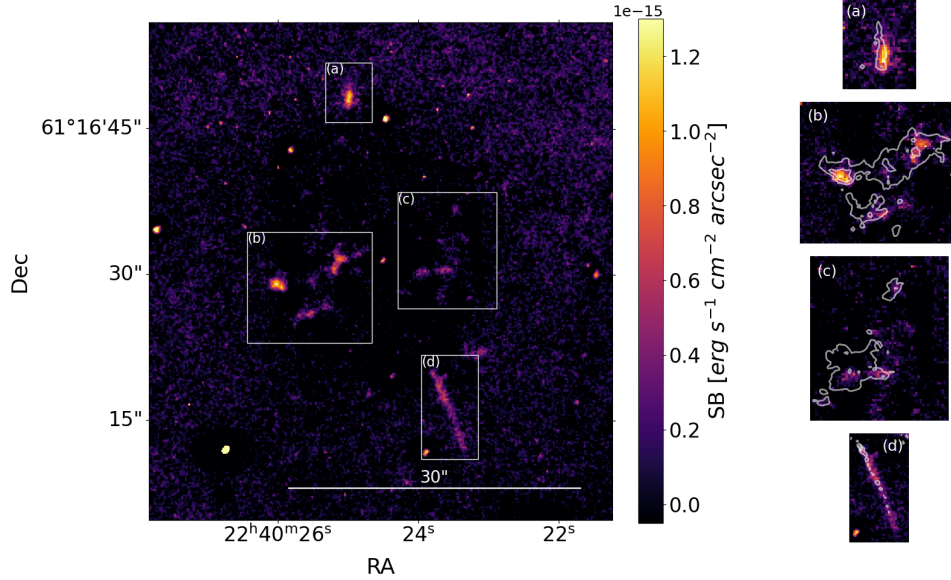


Fig. 6. Surface brightness (SB) of the H_2 1–0 S(1) continuum-subtracted image for NGC 7354 is shown in left panel. The other panels display the H_2 continuum-subtracted image overlaid with HST [N II] emission contours, highlighting for four regions of the nebula: (a) and (d) correspond to the pair of jet-like structures, while (b) and (c) show the equatorial bright LISs.

Wesson et al. (2024) estimated densities of $n_H \sim 10^5 \text{ cm}^{-3}$ and H_2 masses of $\sim 10^{-6} M_\odot$. They noted that, at these densities ($n_{\text{H}_2} = 0.5n_H$), the globules could be in pressure equilibrium with the surrounding ionized gas. Consequently, the globules could remain essentially stable, avoiding collapse or dissipation, until the surrounding gas recombines. On the other hand, De Marco et al. (2022) reported a higher density of $n_H \sim 10^6 \text{ cm}^{-3}$ and an H_2 mass of $\sim 10^{-5} M_\odot$, for the filaments in NGC 3132. These values are 2–3 orders of magnitude higher than the mass of the cometary knot in Helix and 1–2 orders of magnitude greater than our masses in LISs. Although an in-depth comparison of the different structures studied in the referenced works is beyond the scope of this study, we argue that the methodology followed by Matsuura et al. (2007) provides robust estimates for densities and masses.

4.2. Ionized mass

In addition to the warm H_2 component, the ionized mass can also be estimated using near-IR observations, specifically from the flux of the Br γ emission line:

$$F_{\text{Br}\gamma} = 2.77 \times 10^{-28} \frac{n_e^2 V_{\text{HII}}}{d^2}. \quad (3)$$

In Equation 3, assuming that the H II region associated with the H_2 is optically thin in Br γ (Scoville et al. 1982), and adopting case B emissivities from Osterbrock & Ferland (2006), the ionized mass (M_{HII}) can be derived using the equation below:

$$M_{\text{HII}} \sim 3.29 \times 10^{13} \left(\frac{F_{\text{Br}\gamma}}{\text{erg s}^{-1} \text{cm}^{-2}} \right) \left(\frac{d}{\text{kpc}} \right)^2 \left(\frac{n_e}{\text{cm}^{-3}} \right)^{-1} [M_\odot] \quad (4)$$

(Storchi-Bergmann et al. 2009).

Unfortunately, the PNe in our sample were not observed in the Br γ emission line. We then adopt the results in Akra et al. (2017, 2020), who provides fluxes for a number of LISs in four PNe, both for the H_2 1–0 S(1) and Br γ lines, ranging from 0.72 to $21.89 \times 10^{-15} \text{ erg s}^{-1} \text{cm}^{-2}$, and from 0.96 to $94.70 \times 10^{-15} \text{ erg s}^{-1} \text{cm}^{-2}$, respectively. In Table 3, we list the

masses for the warm H_2 gas (obtained from Equation 2), as well as the ionized mass (from Equation 4).

The derivations of the above masses for a reasonable number of LISs allow the construction of the M_{H_2} versus M_{HII} diagram, and also further explore the measurements from Akra et al. (2017, 2020). Nebular components from the PN K 4–47, marked with red dots in Fig. 7, deviate significantly from the bulk of the data and are excluded from both the best-fit mass correlation and further discussion. K 4–47 is a highly collimated PN with a pair of LISs located at the tips of its outflows. Employing photoionization and shock models, it was found that these LISs are likely shock-heated, with shock velocities $\geq 150 \text{ km s}^{-1}$ (Corradi et al. 2000; Gonçalves et al. 2004). In the statistical analysis of LISs and host PNe carried out by Mari et al. (2023a), K 4–47 frequently appear as an outlier – in terms of electron temperatures, chemical abundances and various emission line ratios – showing significant differences from the rest of the LISs.

A significant dispersion ($R^2 \sim 0.48$) is found in the $\log(M_{\text{H}_2})$ – $\log(M_{\text{HII}})$ relation, which probably reflects the large uncertainties in the masses. The best-fit line is represented by:

$$\log(M_{\text{H}_2}) = (0.6 \pm 0.1) \log(M_{\text{HII}}) - (4.6 \pm 0.3) \quad (5)$$

The median M_{HII} for LISs in Table 3, excluding K 4–47, is $7.0 \times 10^{-4} M_\odot$. Using this value in Equation 5, we obtain $M_{\text{H}_2} \sim 3.2 \times 10^{-7} M_\odot$, while the median for this quantity is $3.0 \times 10^{-7} M_\odot$. According to Matsuura et al. (2007), extinction affects the absolute intensity by less than 5%, which does not impact our results or overall conclusions, given that the uncertainty in our mass estimates is even larger. Moreover, following Scoville et al. (1982) and using Equations 1 and 3 for the data in Table 3, we obtain:

$$\frac{M_{\text{HII}}}{M_{\text{H}_2}} = \frac{6.48 \times 10^5}{n_e} \frac{F_{\text{Br}\gamma}}{F_{\text{H}_2, \lambda 2.122}} \quad (6)$$

This corresponds to a difference of only 13 percent compared to Scoville’s ratio (see their Eq. 8). Considering the $F_{\text{Br}\gamma}/F_{\text{H}_2}$ ratio, which ranges from ~ 0.70 to 17.82 , and the median electron density of 2325 cm^{-3} for the LISs in the sample (excluding

Table 2. Position, H₂ 1-0-S(1) fluxes, and molecular masses for various LISs in the studied PNe are presented. The distances required for these calculations were derived from the Gaia DR3 parallax measurements (Gaia Collaboration et al. 2023), yielding the following values: 1.83 kpc for NGC 2392, 3.44 kpc for NGC 6751, 2.86 kpc for NGC 6818 and 2.10 kpc for NGC 7354. For NGC 6884, the distance was adopted from Guerrero et al. (2020) and is 3.2 kpc.

Name	LISs	RA	Dec	Box [arcsec ²]	Flux H ₂ 1-0 S(1) [$\times 10^{-15}$ erg s ⁻¹ cm ⁻²]	H ₂ M _{warm} [$\times 10^{-07}$ M _⊙]
NGC 2392	1	07:29:11.54	+20:54:34.22	0.896 \times 0.478	0.25	0.4
	2	07:29:11.84	+20:54:39.48	1.499 \times 0.483	0.38	0.6
	3	07:29:11.66	+20:54:50.73	1.396 \times 0.551	0.37	0.6
	4	07:29:10.32	+20:54:56.62	0.710 \times 1.464	0.80	1.4
	5	07:29:09.90	+20:54:53.93	0.539 \times 1.903	0.53	0.9
NGC 6751	1	19:05:56.60	-05:59:36.90	1.273 \times 1.272	0.37	2.2
	2	19:05:56.46	-05:59:37.21	1.992 \times 1.632	0.75	4.5
	3	19:05:56.08	-05:59:39.95	1.692 \times 1.549	1.04	6.2
	4	19:05:55.80	-05:59:37.22	0.873 \times 3.375	1.10	6.6
	5	19:05:55.80	-05:59:29.84	1.832 \times 2.208	1.73	10.4
	H1 [§]	19:05:58.37	-05:59:47.58	1.413 \times 2.194	2.26	13.6
	H2 [§]	19:05:52.57	-05:59:42.75	1.317 \times 2.348	3.84	23.1
	H3 [§]	19:05:52.52	-05:59:48.79	1.409 \times 2.584	2.27	13.6
	H4 [§]	19:05:58.41	-05:59:32.30	1.351 \times 1.377	1.85	11.1
NGC 6818	1	19:43:57.94	-14:09:09.37	1.229 \times 2.517	1.44	6.0
	2	19:43:57.51	-14:09:17.69	1.418 \times 4.050	2.39	10.0
	3	19:43:57.91	-14:09:21.85	1.497 \times 2.761	2.17	9.0
NGC 6884	1	20:10:23.72	+46:27:37.68	0.545 \times 1.468	1.86	9.7
	2	20:10:23.75	+46:27:36.39	0.616 \times 0.992	0.75	3.9
	H1 [§]	20:10:21.02	+46:28:00.16	2.000 \times 2.000	6.67	34.7
	H2 [§]	20:10:20.68	+46:27:55.67	3.000 \times 3.000	18.35	95.4
	H3 [§]	20:10:25.64	+46:27:31.87	2.000 \times 2.000	2.60	13.5
	H4 [§]	20:10:26.57	+46:27:28.04	3.000 \times 3.000	6.91	35.9
NGC 7354	1	22:40:20.12	+61:17:23.82	0.984 \times 2.349	1.35	3.0
	2	22:40:21.13	+61:17:04.84	1.389 \times 1.784	1.41	3.1
	3	22:40:18.66	+61:16:52.00	1.553 \times 10.70	2.69	6.0
	4	22:40:20.28	+61:17:06.98	1.559 \times 2.940	1.47	3.3
Helix Nebula	†K1	†22:29:33.41	†-20:48:04.73	†2 \times 2	†1.88 $\times 10^{-14}$	3.9 $\times 10^{-08}$ †2 $\times 10^{-08}$

Notes. The last row corresponds to another LIS, a cometary knot of Helix nebula, for comparison purposes.

[§] Structures found in the nebular halo.

[†]The average intensity over 2 \times 2 arcsec² and the H₂ warm mass, are from Matsuura et al. (2007).

K 4-47), we find that their ionized masses (M_{HII}) are between approximately 200 to 5000 times larger than the warm molecular hydrogen masses (M_{H_2}).

5. Discussion

Since this work presents the first near-IR H₂ 1-0 2.122 μ m detections in the LISs of NGC 2392, NGC 6751, NGC 6818, NGC 6884 and NGC 7354, we begin by briefly characterizing these structures where warm molecular hydrogen was detected.

(i) Multiple system of knotty and filamentary LISs, located at the inner part of the shell, in the high-excitation PN NGC 2392. It also displays high-velocity ([N II]) jets directed toward the observer but not detected in H₂ (García-Díaz et al. 2012; Guerrero et al. 2021). The electron densities of the knots and filaments are 900-1000 cm⁻³, 2 to 3 times lower than the electron densities in the nebular shell, while T_e does not vary significantly (Barker 1991; Zhang et al. 2012).

(ii) Although NGC 6751 displays a large halo in which H₂ is also detected (Clark et al. 2010), the clumpy LISs of its inner regions, including the jet-like structures (ansae, in Chu et al. 1991) are the main focus here. T_e has been found to be similar across the different nebular regions. On the other hand, the jet-like structures,

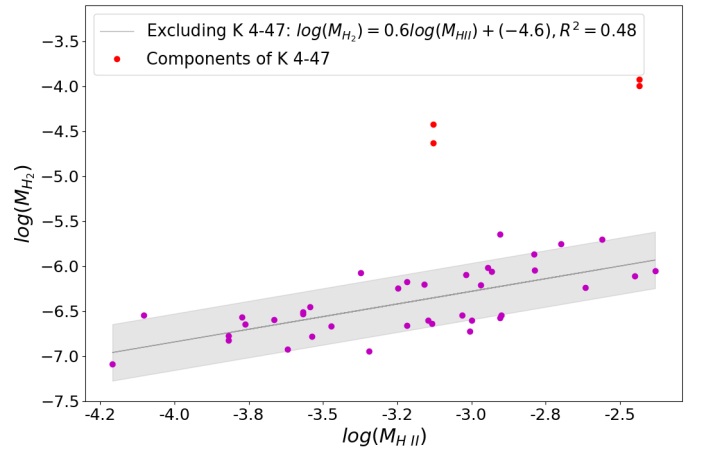


Fig. 7. Correlation between ionized and warm molecular hydrogen mass for the LISs present in NGC 7662, NGC 7009 and NGC 6543 (Akras et al. 2017, 2020). The gray filled area represents the uncertainty of the regression line. LISs and outflows from K 4-47 were excluded from the linear fit due to their significant deviation from the bulk. The red points correspond to these nebular components, with the more massive ones representing the outflows.

Table 3. Positions, H₂ 1-0-S(1) and Bry fluxes, warm molecular and ionized masses for various LISs in K 4-47 and NGC 7662 (Akraś et al. 2017), as well as NGC 7009 and NGC 6543 (Akraś et al. 2020), are presented. For PNe with multiple LISs, an average value of electron densities (n_e) was used, based on the published measurements for the LISs in each object. The n_e were adopted from Gonçalves et al. (2004) for K 4-47, Gonçalves et al. (2009) for NGC 7662, Gonçalves et al. (2003) for NGC 7009 and Balick et al. (1994) for NGC 6543.

Name	LISs	RA	Dec	Flux H ₂ 1-0-S(1) [$\times 10^{-15}$ erg s ⁻¹ cm ⁻²]	Flux Bry [$\times 10^{-15}$ erg s ⁻¹ cm ⁻²]	n_e [cm ⁻³]	M_{warm} [$\times 10^{-07}$ M _⊙]	M_{ion} [$\times 10^{-04}$ M _⊙]
K 4-47	1	04:20:45.5	+56:18:16.2	6.82	0.96	4600	375	7.4
	2	04:20:44.9	+56:18:10.6	4.29	0.96	4600	236	7.4
	3 [†]	04:20:45.4	+56:18:14.8	21.89	2.47	2400	1202	36.6
	4 [†]	04:20:45.1	+56:18:12.4	18.38	2.47	2400	1009	36.6
NGC 7662	1	23:25:54.7	+42:32:21.5	1.88	6.18	2325	3.0	2.7
	2	23:25:54.5	+42:32:21.6	1.96	6.18	2325	3.1	2.7
	3	23:25:54.6	+42:32:17.5	1.05	6.62	2325	1.7	2.9
	4	23:25:54.6	+42:32:16.2	4.23	13.80	2325	6.7	6.0
	5	23:25:54.4	+42:32:14.8	5.14	21.90	2325	8.1	9.6
	6	23:25:54.7	+42:32:15.4	1.38	7.68	2325	2.2	3.4
	7	23:25:54.8	+42:32:13.8	8.63	37.10	2325	13.6	16.3
	8	23:25:54.9	+42:32:09.7	12.60	62.80	2325	19.8	27.5
	9	23:25:54.9	+42:32:09.1	3.95	24.50	2325	6.2	10.7
	10	23:25:54.4	+42:32:10.9	1.61	4.94	2325	2.5	2.2
	11	23:25:54.6	+42:32:09.6	1.44	3.94	2325	2.3	1.7
	12	23:25:54.5	+42:32:07.6	1.73	3.85	2325	2.7	1.7
	13	23:25:54.7	+42:32:06.7	1.81	21.20	2325	2.8	9.3
	14	23:25:54.8	+42:32:05.4	1.59	16.30	2325	2.5	7.1
	15	23:25:54.9	+42:32:05.5	1.39	13.80	2325	2.2	6.0
	16	23:25:54.9	+42:32:01.2	1.69	28.40	2325	2.7	12.4
	17	23:25:54.7	+42:32:00.3	1.59	22.90	2325	2.5	10.0
	18	23:25:54.6	+42:31:58.7	1.46	16.80	2325	2.3	7.4
	19	23:25:53.7	+42:31:58.2	5.62	94.70	2325	8.8	41.5
	20	23:25:53.7	+42:31:57.3	4.95	80.90	2325	7.8	35.5
	21	23:25:53.7	+42:31:52.0	14.30	28.40	2325	22.5	12.4
	22	23:25:53.6	+42:31:50.4	5.38	9.67	2325	8.5	4.2
	23	23:25:53.5	+42:31:48.2	0.96	3.47	2325	1.5	1.5
	24	23:25:53.5	+42:31:47.3	1.07	3.47	2325	1.7	1.5
	25	23:25:53.2	+42:32:02.9	5.72	37.20	2325	9.0	16.3
	26	23:25:52.9	+42:32:01.5	2.26	6.51	2325	3.6	2.9
	27	23:25:52.9	+42:31:57.6	11.20	45.70	2325	17.6	20.0
	28	23:25:53.2	+42:31:54.8	6.09	25.90	2325	9.6	11.4
	29	23:25:54.2	+42:32:18.8	0.72	10.30	2325	1.1	4.5
NGC 7009	1	21:04:12.5	-11:21:41.9	3.71	2.61	1650	2.9	0.8
	2	21:04:12.7	-11:21:36.8	1.06	2.05	1650	0.8	0.6
	3	21:04:09.0	-11:21:52.9	11.40	28.20	1200	8.8	11.7
	4	21:04:09.0	-11:21:53.2	8.13	16.70	1200	6.2	6.9
	5	21:04:09.0	-11:21:52.9	7.36	13.60	1200	5.7	5.6
NGC 6543	1	17:58:32.1	+66:37:47.7	2.99	44.80	2200	2.8	12.6
	2	17:58:32.1	+66:37:47.4	6.03	86.30	2200	5.7	24.2
	3	17:58:32.2	+66:37:46.9	1.26	8.56	2200	1.2	2.4
	4	17:58:33.8	+66:38:11.7	1.97	35.10	2200	1.9	9.9

Notes. [†] Outflows from K 4-47 (Akraś et al. 2017), although showing H₂ emission, are not considered LISs.

knots and rim have, respectively, ~ 200 cm⁻³, ~ 1600 cm⁻³ and ~ 2500 cm⁻³ (Chu et al. 1991).

(iii) NGC 6818 has multiple [N II]-bright filamentary structures distributed throughout the nebula ("moustaches", Benetti et al. 2003), which are also observed in H₂. These structures are peculiar due to their higher kinematics gradients (Hyung et al. 1999) and electron densities compared to the other nebular components. Across the nebula, N_e [S II] varies between 1500 and 2800 cm⁻³, with the equatorial filamentary structures being the densest regions (Benetti et al. 2003; Tsamis et al. 2003; Pottasch et al. 2005).

(iv) [N II] HST images and H₂ NIRC2 images have revealed that the LISs of NGC 6884 form a pair of knotty, arc-like structures (Palen et al. 2002). T_e show a slight vari-

ation between the low- (~ 8500 K) and moderate-ionization (~ 10000 K) regions of the nebula. The low-ionization regions have $N_e[\text{O II}]_{\text{of}} \sim 16000 \text{ cm}^{-3}$ while, based on $[\text{A IV}]$ and $[\text{Cl III}]$ diagnostics, the rest of the nebula has values of $\sim 6000 \text{ cm}^{-3}$ (Hyung et al. 1997).

(v) The equatorial knots and jet-like structures of NGC 7354, detected in H_2 , were studied by Hajian et al. (1997); Contreras et al. (2010), who derived their temperatures and densities. The pair of jet-like structures, equatorial knots, and high-ionization shell are characterized by $N_e (T_e)$ values of $\sim 970 \text{ cm}^{-3}$ (10000-12000 K), $\sim 3000 \text{ cm}^{-3}$ (10000-13000 K), $1500\text{-}2600 \text{ cm}^{-3}$ ($\sim 10000\text{-}13000$ K), respectively.

Regardless of their physical conditions, the nebular components or LISs, where H_2 emission is unambiguously detected, are associated with structures that are prominent in the $[\text{N II}]$ emission line. In most cases, the H_2 detections are associated with structures that, relative to the rims and shells of their host nebulae, have lower electron densities. Thus, by doubling the sample of known PNe with LISs detected in H_2 line, we verify that LISs are indeed composed of partially ionized and excited molecular gas. In addition to the LISs, which were the main focus of this narrowband survey, H_2 emission was also detected for the first time in the halos of NGC 6751 and NGC 6884.

Moreover, for the first time, the molecular mass of excited (warm) H_2 gas in LISs was estimated for our sample of five PNe, along with the LISs in four PNe from the literature. The corresponding ionized masses of these LISs were also calculated. Based on the range of near-IR H_2 and $\text{Br}\gamma$ fluxes reported by Akas et al. (2017, 2020), we found that the ionized mass in LISs is between 200 and 5000 times greater than the excited molecular mass.

As mentioned in Section 4, our data do not represent the distribution of the cold molecular component, but only the warm component. Estimating the H_2 mass of the cold counterpart is commonly done through CO emission. However, this method requires converting the CO column density into H_2 mass, and for this, it is necessary to assume a conversion factor for the CO/ H_2 ratio – a highly uncertain quantity (see, e.g., Bolatto et al. 2013).

No actual measurements of the mass of the cold components are available for the LISs discussed in the present work due to the lack of any CO detection so far. Andriantsaralaza et al. (2020) analyzed ALMA CO observations of a globule in the Helix nebula, specifically the C1 globule previously detected in CO and H_2 by Huggins et al. (2002). Using CO emission lines as H_2 tracers, the molecular mass of the globule’s head has been estimated ($0.8 - 1.3$) $\times 10^{-5} M_\odot$ (Andriantsaralaza et al. 2020) and $\approx 1 \times 10^{-5} M_\odot$ (Huggins et al. 2002), assuming a CO/ H_2 ratio of $\sim 10^{-4}$ Huggins et al. (1992, 2002). Considering the H_2 $2.122 \mu\text{m}$ flux reported by Huggins et al. (2002) at the globule’s head (whereas the tail was significantly fainter in this emission), we estimated the warm molecular mass using Equation 2 to be $\sim 1.5 \times 10^{-8} M_\odot$. This suggests that the cold H_2 mass in the C1 head is approximately $5.3 - 8.7 \times 10^2$ times greater than the warm H_2 mass, yielding a mean ratio of $M_{\text{cold}}/M_{\text{warm}} \sim 7 \times 10^2$. Based on this, if a cold H_2 gas component is present in our sample of LISs, their masses should range between $(0.3 - 7.3) \times 10^{-4} M_\odot$, with a mean value of $3.8 \times 10^{-4} M_\odot$. This is approximately half of the median ionized mass found for LISs in Section 4.2.

Since no other LISs have been detected in both H_2 and CO so far, direct comparisons are not possible. Nevertheless, the cold H_2 mass in the nebula NGC 3132 has also been computed based on Submillimeter Array (SMA) observations, ranging between

~ 0.015 and $\sim 0.15 M_\odot$, assuming a CO/ H_2 conversion factor between 10^{-4} and 10^{-5} (Kastner et al. 2024).

The presence of molecular gas in LISs offers new insight to better understand their origin and nature. The new detections of H_2 emission from LISs have doubled the total number of PNe (nine in total) with LISs directly associated with warm molecular gas. This provides further support for the scenario in which LISs may represent mini-photodissociation regions (PDRs) illuminated by the hard UV radiation from the central stars of PNe. Nevertheless, it should be noted that the potential PDRs at the surfaces of LISs may differ from the PDRs typically found in high-mass star-forming regions (Hollenbach & Tielens 1997). The very low ionization parameters of PNe’ LISs may cause the ionization and dissociation fronts of H_2 to merge (Bertoldi & Draine 1996; Henney et al. 2007).

The survival of molecular gas in these nebular structures raises an important question: *how does it survive the dissociation due to the energetic UV photons of the central star?* Recent detection of the $[\text{C I}] \lambda 8727$ emission line from the LISs of NGC 7009 (Akas et al. 2024) and NGC 3242 (Konstantinou et al. 2025) suggests the photoevaporation of the molecular gas, which becomes dissociated and ionized as it flows away from the knots. Akas et al. (2024) demonstrated, at least for the northeastern LIS of NGC 7009, a stratified ionization structure at the interface between the outer ionized gas and the dense molecular core (i.e. within a transition zone). The emission profiles of that LIS show $[\text{C I}]$ arising between $[\text{N II}]$ and H_2 , which contrasts with what is observed in PDRs of star-forming regions (e.g. Henney 2021).

As mentioned before, the physical conditions in LISs may deviate significantly from those of typical high-mass star-forming PDRs. Nevertheless, LISs appear to preserve some key features of typical PDRs, such as a stratified emission region, high total densities, and low temperatures. Hollenbach & Tielens (1997) depicted a schematic of a PDR structure, where the H II component is followed by a thin $\text{H II}/\text{H I}$ layer that absorbs Lyman-continuum photons. These layers are followed by large column densities of O, C, C^+ , CO and vibrationally excited H_2 . The typical total densities (10^{3-5} cm^{-3}) and temperatures (between 200 and 1000 K) of PDRs are comparable to those mentioned by Balick et al. (2020), where the authors have predicted high densities (10^{6-7} cm^{-3}) and low temperatures (3×10^{-3} K) in the interior of LISs. Such high densities has also been suggested for the LISs in NGC 6720 and NGC 3132 (Wesson et al. 2024; De Marco et al. 2022).

6. Conclusion

In this study we presented a deep narrowband H_2 imaging study of five PNe with several LISs embedded. The number of PNe with LISs detected in the near-IR H_2 $2.122 \mu\text{m}$ ro-vibrational line has doubled (to 9). The conclusions of the study are as follows:

- Although the detected emission corresponds to warm H_2 , it directly implies the presence of a colder molecular component. The coexistence of warm and cold H_2 supports the model expectations that LISs contain significant amounts of molecular material, helping reconcile the low *electron* densities derived from the ionized gas with models that predict total densities in LISs to be orders of magnitude higher than in the host nebula;
- The warm H_2 masses of the LISs studied in this work range from 0.4 to $10 \times 10^{-7} M_\odot$, with an average of $4.6 \times 10^{-7} M_\odot$;

- The ionized masses (M_{HII}) of the LISs observed in Br γ vary between 0.6 and $41.5 \times 10^{-4} M_{\odot}$, with an average value of $7 \times 10^{-4} M_{\odot}$;
- We found that the excited H $_2$ molecular mass (M_{H_2}) in LISs is between 200 and 5000 times lower than the corresponding ionized mass.

Acknowledgements. We thank William Henney, the referee, for his comments and suggestions. We would like to thank Mateus Dias Ribeiro for his essential help with techniques to degrade the images to improve the continuum subtraction and the so reliable result. This research project was partially supported by the Consejo Nacional de Investigaciones Científicas y Técnicas (CONICET, Argentina). MBM was supported by a CAPES (The Brazilian Federal Agency for Support and Evaluation of Graduate Education within the Education Ministry) fellowship at the beginning of this study. SA acknowledges the research project implemented in the frame-work of H.F.R.I call “Basic research financing (Horizontal support of all Sciences)” under the National Recovery and Resilience Plan “Greece 2.0” funded by the European Union – NextGenerationEU (H.F.R.I. Project Number: 15665). DRG acknowledges FAPERJ (E-26/211.527/2023) and CNPq (315307/2023-4) for partial support. This research is based on observations acquired through the Gemini Observatory Archive at NSF NOIRLab and processed using DRAGONS (Data Reduction for Astronomy from Gemini Observatory North and South). This work makes use of Hubble Space Telescope data obtained from the Hubble Legacy Archive (STScI/NASA, ST-ECF/ESA, CADR/NRC/CSA).

References

- Akras, S. & Gonçalves, D. R. 2016, *MNRAS*, 455, 930
- Akras, S., Gonçalves, D. R., & Ramos-Larios, G. 2017, *MNRAS*, 465, 1289
- Akras, S., Gonçalves, D. R., Ramos-Larios, G., & Aleman, I. 2020, *MNRAS*, 493, 3800
- Akras, S., Monteiro, H., Walsh, J. R., et al. 2022, *MNRAS*, 512, 2202
- Akras, S., Monteiro, H., Walsh, J. R., et al. 2024, *A&A*, 689, A14
- Aleman, I. & Gruenwald, R. 2011, *A&A*, 528, A74
- Ali, A. & Dopita, M. A. 2017, *PASA*, 34, e036
- Andriantsaralaza, M., Zijlstra, A., & Avison, A. 2020, *MNRAS*, 491, 758
- Bailer-Jones, C. A. L., Rybizki, J., Fouesneau, M., Demleitner, M., & Andrae, R. 2021, *AJ*, 161, 147
- Balick, B., Alexander, J., Hajian, A. R., et al. 1998, *AJ*, 116, 360
- Balick, B. & Frank, A. 2002, *Annual Review of Astronomy and Astrophysics*, 40, 439
- Balick, B., Frank, A., & Liu, B. 2020, *ApJ*, 889, 13
- Balick, B., Perinotto, M., Maccioni, A., Terzian, Y., & Hajian, A. 1994, *ApJ*, 424, 800
- Barker, T. 1991, *ApJ*, 371, 217
- Benetti, S., Cappellaro, E., Ragazzoni, R., Sabbadin, F., & Turatto, M. 2003, *A&A*, 400, 161
- Bertoldi, F. 1989, *ApJ*, 346, 735
- Bertoldi, F. & Draine, B. T. 1996, *ApJ*, 458, 222
- Bertoldi, F. & McKee, C. F. 1990, *ApJ*, 354, 529
- Bolatto, A. D., Wolfire, M., & Leroy, A. K. 2013, *ARA&A*, 51, 207
- Cardelli, J. A., Clayton, G. C., & Mathis, J. S. 1989, *ApJ*, 345, 245
- Chu, Y.-H., Manchado, A., Jacoby, G. H., & Kwitter, K. B. 1991, *ApJ*, 376, 150
- Clark, D. M., García-Díaz, M. T., López, J. A., Steffen, W. G., & Richer, M. G. 2010, *ApJ*, 722, 1260
- Contreras, M. E., Vázquez, R., Miranda, L. F., et al. 2010, *AJ*, 139, 1426
- Corradi, R. L. M., Gonçalves, D. R., Villaver, E., et al. 2000, *ApJ*, 535, 823
- Corradi, R. L. M., Manso, R., Mampaso, A., & Schwarz, H. E. 1996, *A&A*, 313, 913
- Danehkar, A., Parker, Q. A., & Steffen, W. 2016, *AJ*, 151, 38
- De Marco, O., Akashi, M., Akas, S., et al. 2022, *Nature Astronomy*, 6, 1421
- Diniz, M. R., Riffel, R. A., Storch-Bergmann, T., & Winge, C. 2015, *MNRAS*, 453, 1727
- Fang, X., Guerrero, M. A., Miranda, L. F., et al. 2015, *MNRAS*, 452, 2445
- Fang, X., Zhang, Y., Kwok, S., et al. 2018, *ApJ*, 859, 92
- Gaia Collaboration, Vallenari, A., Brown, A. G. A., et al. 2023, *A&A*, 674, A1
- García-Díaz, M. T., López, J. A., Steffen, W., & Richer, M. G. 2012, *ApJ*, 761, 172
- García-Rojas, J., Morisset, C., Jones, D., et al. 2022, *MNRAS*, 510, 5444
- Giesekeing, F., Becker, I., & Solf, J. 1985, *Astrophys. J. Let.*, 295, L17
- Gonçalves, D. R., Corradi, R. L. M., & Mampaso, A. 2001, *ApJ*, 547, 302
- Gonçalves, D. R., Corradi, R. L. M., Mampaso, A., & Perinotto, M. 2003, *ApJ*, 597, 975
- Gonçalves, D. R., Mampaso, A., Corradi, R. L. M., et al. 2004, *MNRAS*, 355, 37
- Gonçalves, D. R., Mampaso, A., Corradi, R. L. M., & Quireza, C. 2009, *MNRAS*, 398, 2166
- Guerrero, M. A., Cazzoli, S., Rechy-García, J. S., et al. 2021, *ApJ*, 909, 44
- Guerrero, M. A., Suzett Rechy-García, J., & Ortiz, R. 2020, *ApJ*, 890, 50
- Hajian, A. R., Balick, B., Terzian, Y., & Perinotto, M. 1997, *ApJ*, 487, 304
- Hambly, N. C., Collins, R. S., Cross, N. J. G., et al. 2008, *MNRAS*, 384, 637
- Henney, W. J. 2021, *MNRAS*, 502, 4597
- Henney, W. J., Williams, R. J. R., Ferland, G. J., Shaw, G., & O’Dell, C. R. 2007, *ApJ*, 671, L137
- Hollenbach, D. J. & Tielens, A. G. G. M. 1997, *ARA&A*, 35, 179
- Hora, J. L., Latter, W. B., Smith, H. A., & Marengo, M. 2006, *ApJ*, 652, 426
- Huggins, P. J., Bachiller, R., Cox, P., & Forveille, T. 1992, *ApJ*, 401, L43
- Huggins, P. J., Forveille, T., Bachiller, R., et al. 2002, *ApJ*, 573, L55
- Hyung, S., Aller, L. H., & Feibelman, W. A. 1997, *ApJS*, 108, 503
- Hyung, S., Aller, L. H., & Feibelman, W. A. 1999, *ApJ*, 514, 878
- Kahn, F. D. 1954, *Bull. Astron. Inst. Netherlands*, 12, 187
- Kastner, J. H., Weintraub, D. A., Gatley, I., Merrill, K. M., & Probst, R. G. 1996, *ApJ*, 462, 777
- Kastner, J. H., Wilner, D. J., Moraga Baez, P., et al. 2024, *ApJ*, 965, 21
- Konstantinou, L., Akas, S., Garcia-Rojas, J., et al. 2025, *A&A*, 697, A227
- Labrie, K., Anderson, K., Cárdenes, R., Simpson, C., & Turner, J. E. H. 2019, in *Astronomical Society of the Pacific Conference Series*, Vol. 523, *Astronomical Data Analysis Software and Systems XXVII*, ed. P. J. Teuben, M. W. Pound, B. A. Thomas, & E. M. Warner, 321
- Lawrence, A., Warren, S. J., Almaini, O., et al. 2007, *MNRAS*, 379, 1599
- López-Martín, L., Raga, A. C., Mellema, G., Henney, W. J., & Cantó, J. 2001, *ApJ*, 548, 288
- Manchado, A., Stanghellini, L., & Guerrero, M. A. 1996, *ApJ*, 466, L95
- Mari, M. B., Akas, S., & Gonçalves, D. R. 2023a, *MNRAS*, 525, 1998
- Mari, M. B., Gonçalves, D. R., & Akas, S. 2023b, *MNRAS*, 518, 3908
- Matsuura, M., Speck, A. K., McHunu, B. M., et al. 2009, *ApJ*, 700, 1067
- Matsuura, M., Speck, A. K., Smith, M. D., et al. 2007, *MNRAS*, 382, 1447
- Meixner, M., McCullough, P., Hartman, J., Son, M., & Speck, A. 2005, *AJ*, 130, 1784
- Mellema, G., Raga, A. C., Canto, J., et al. 1998, *A&A*, 331, 335
- Miranda, L. F., Guerrero, M. A., & Torrelles, J. M. 1999, *AJ*, 117, 1421
- Miranda, L. F., Suárez, O., Olguín, L., et al. 2021, *arXiv e-prints*, arXiv:2105.05186
- Monreal-Ibero, A. & Walsh, J. R. 2020, *A&A*, 634, A47
- O’Dell, C. R. & Ball, M. E. 1985, *ApJ*, 289, 526
- O’Dell, C. R. & Handron, K. D. 1996, *AJ*, 111, 1630
- O’Dell, C. R., Henney, W. J., & Burkert, A. 2000, *AJ*, 119, 2910
- O’Dell, C. R., Henney, W. J., & Ferland, G. J. 2005, *AJ*, 130, 172
- Oort, J. H. & Spitzer, Jr., L. 1955, *ApJ*, 121, 6
- Osterbrock, D. E. & Ferland, G. J. 2006, *Astrophysics of gaseous nebulae and active galactic nuclei* (-)
- Palen, S., Balick, B., Hajian, A. R., et al. 2002, *AJ*, 123, 2666
- Phillips, J. P., Ramos-Larios, G., Schröder, K. P., & Contreras, J. L. V. 2009, *MNRAS*, 399, 1126
- Pottasch, S. R., Beintema, D. A., & Feibelman, W. A. 2005, *A&A*, 436, 953
- Raga, A. C., Riera, A., Mellema, G., Esquivel, A., & Velázquez, P. F. 2008, *A&A*, 489, 1141
- Raga, A. C., Steffen, W., & González, R. F. 2005, *Rev. Mexicana Astron. Astrofis.*, 41, 45
- Ramos-Larios, G. & Phillips, J. P. 2009, *MNRAS*, 400, 575
- Reay, N. K., Walton, N. A., & Atherton, P. D. 1988, *MNRAS*, 232, 615
- Reunanen, J., Kotilainen, J. K., & Prieto, M. A. 2002, *MNRAS*, 331, 154
- Riffel, R. A., Storch-Bergmann, T., Winge, C., et al. 2008, *MNRAS*, 385, 1129
- Scoville, N. Z., Hall, D. N. B., Ridgway, S. T., & Kleinmann, S. G. 1982, *ApJ*, 253, 136
- Skrutskie, M. F., Cutri, R. M., Stiening, R., et al. 2006, *AJ*, 131, 1163
- Steffen, W., López, J. A., & Lim, A. 2001, *ApJ*, 556, 823
- Storch-Bergmann, T., McGregor, P. J., Riffel, R. A., et al. 2009, *MNRAS*, 394, 1148
- Tsamis, Y. G., Barlow, M. J., Liu, X. W., Danziger, I. J., & Storey, P. J. 2003, *MNRAS*, 345, 186
- Turner, J., Kirby-Docken, K., & Dalgarno, A. 1977, *ApJS*, 35, 281
- Wesson, R., Matsuura, M., Zijlstra, A. A., et al. 2024, *MNRAS*, 528, 3392
- Zhang, Y., Fang, X., Chau, W., et al. 2012, *ApJ*, 754, 28